

Flexible Perovskite X-Ray Detectors through Interfacial Modification with Perylene Diimide

He Zhao, Jian Qiu, Bo Hou, Luying Yi, Xian Qin, and Xiaogang Liu*

Flexible direct X-ray detectors based on perovskites have great potential for X-ray imaging due to their high sensitivity, low detection limit, low-cost, and large-area fabrication. However, these detectors perform inefficiently at X-ray-to-current conversion because of inadequate functional layer thickness and charge-carrier recombination. Here, the fabrication of an integrated, self-powered X-ray detector based on CsPbBr₃ quantum dots and a MAPbI₃ photoelectric conversion layer embedded with perylene diimide molecules is reported. In addition to optimizing crystal domain formation and charge carrier extraction, the perylene diimide molecules also improve the electron mobility of MAPbI₃ films by twofold. The integrated perovskite-based X-ray detector has a sensitivity of $143\,169 \pm 848 \mu\text{C Gy}_{\text{air}}^{-1} \text{cm}^{-2}$ and a detection limit of 30.77 nGy s^{-1} . The perylene diimide molecule at the grain boundary of MAPbI₃ shows defect passivation and charge collection characteristics, leading to stable output over 30 bending cycles. This hybrid molecular approach provides insight into a general method to modify device performance using perylene diimide-integrated detectors for X-ray imaging of 3D objects with curved surfaces.

1. Introduction

Flexible X-ray detectors have gained popularity in recent years because their ability to image 3D objects with irregular shapes and reduce the size of the imaging system.^[1,2] Moreover, the image quality of flexible devices is better than that of flat-panel detectors because the image distortion is lower and each pixel of the detectors can be irradiated with a relatively uniform dose.^[1] Therefore, flexible detectors with curved surfaces are preferred for X-ray imaging. The majority of commercial X-ray imaging equipment utilizes amorphous selenium photodetectors or scintillator-based flat-panel detectors. However, flexible or curved X-ray detectors are difficult to fabricate due to the rigidity and inflexibility of conventional flat-panel photodetectors.

H. Zhao, J. Qiu, X. Liu
Joint School of National University of Singapore and Tianjin University
International Campus of Tianjin University
Binhai New City, Fuzhou 350207, P. R. China
E-mail: chmlx@nus.edu.sg

H. Zhao, J. Qiu, B. Hou, L. Yi, X. Qin, X. Liu
Department of Chemistry
National University of Singapore
Singapore 117543, Singapore

 The ORCID identification number(s) for the author(s) of this article can be found under <https://doi.org/10.1002/adom.202202668>.

DOI: 10.1002/adom.202202668

In the past decade, metal-halide perovskites have shown good potential for ionizing radiation detection due to their high X-ray absorption coefficient and high carrier mobility. Many research groups have developed flexible direct X-ray detectors or integrated indirect devices based on perovskite semiconductor thin films.^[3] Although these perovskite-based devices have presented better performance than commercial detectors, the efficiency of converting X-rays to current in these devices is still quite low due to the insufficient thickness of the functional layer and considerable charge-carrier recombination.^[4]

In this work, we report the use of perylene diimide to overcome the limitations associated with conventional perovskite-based flexible X-ray detectors. Perylene diimide is a molecular electron acceptor (n-type semiconductor) with intense light absorption, high stability, and unity quantum yield. Because of these properties, perylene diimide has been widely used in photoelectric devices, organic field-effect transistors, and energy-transfer cascades.^[5] Using these molecules, we expect to improve charge transfer dynamics and enhance X-ray detection.

2. Results and Discussion

In a typical experiment, we synthesized *N*-bis-ethylamine-peryrene-3,4,9,10-tetracarboxylic-diimide hydriodate (PDI-EAI) by adding an alkylamine group to perylene diimide to weaken the π - π interaction and improve the dispersivity in the perovskite precursor (Scheme S1 and Figure S1, Supporting Information). The UV-vis absorption of PDI-EAI in dimethyl sulfoxide showed strong absorption in the range of 500–550 nm (Figure 1a). According to Planck's equation, the band gap energy of PDI-EAI was determined to be 2.24 eV from the wavelength of the intersection between absorption and photoluminescence spectra. The lowest unoccupied molecular orbital (LUMO) energy level of PDI-EAI was evaluated by cyclic voltammetry (Figure 1b). In the cathodic scan, PDI-EAI showed two reversible reduction peaks, representing the first and second stepwise reduction processes with one electron. The onset of the first reduction potential (E^{red}) of the molecule is at -0.34 V . Hence, the LUMO energy level of PDI-EAI is estimated to be -3.87 eV using the empirical formula.^[6]

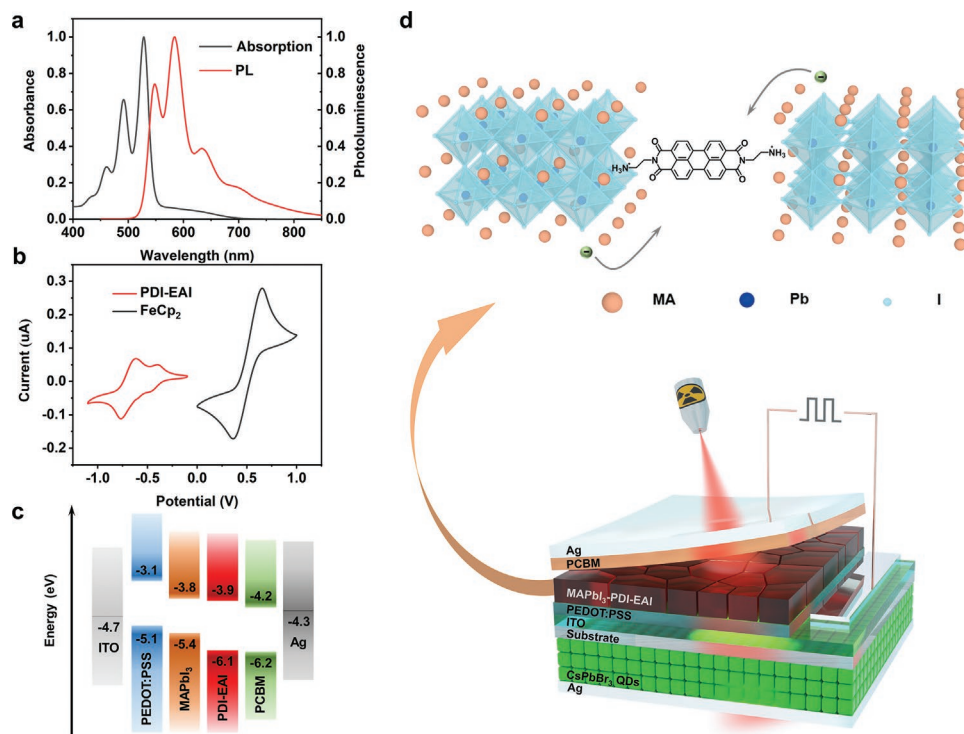


Figure 1. a) UV-vis absorption and PL spectrum of a PDI-EAI solution. b) Cyclic voltammograms of PDI-EAI and FeCp₂ in dimethyl sulfoxide with *n*-Bu₄NPF₆ as a supporting electrolyte. c) Schematic energy level diagram of the MAPbI₃, PDI-EAI, and PCBM. d) The device structure of a perovskite-based flexible integrated X-ray detector.

$$E_{\text{LUMO}} = -[E_{\text{Fc}/\text{Fc}^+}^{\text{red}} - E_{\text{Fc}/\text{Fc}^+}^{\text{red}} + 4.8] \quad (1)$$

where $E_{\text{Fc}/\text{Fc}^+}^{\text{red}}$ is the onset reduction potential of ferrocene (0.59 V), 4.8 is the difference between the vacuum energy level, and the absolute energy level of FeCp₂⁺⁰. In accordance with the optical band gap of PDI-EAI, the highest occupied molecular orbital (HOMO) of PDI-EAI is -6.1 eV by subtracting the band gap from LUMO. We compared the energy levels of MAPbI₃, PDI-EAI, and phenyl-C61-butryric acid methyl ester (PCBM, Figure 1c). The conduction band minimum of the perovskite is slightly higher than the LUMO of PDI-EAI, which is higher than the LUMO of PCBM. Therefore, the photoelectron can be transported from the perovskite to PDI-EAI and then to PCBM without an energy barrier.^[7]

The PDI-EAI-modified detector adopts a multilayer p-i-n structure with Ag/LiF/PCBM/PDI-EAI-modified MAPbI₃/poly(3,4-ethylenedioxythiophene) polystyrene sulfonate (PEDOT:PSS)/indium-doped tin oxide (ITO)/polyethylene terephthalate (PET)/CsPbBr₃ quantum dots/Ag (Figure 1d). When X-rays strike the MAPbI₃ layer, a small fraction of the high-energy photons can be directly converted into charge carriers, while most of the transmitted X-rays are down-converted into visible light by CsPbBr₃ quantum dots, which can be further collected by MAPbI₃.

Upon X-ray irradiation, CsPbBr₃ quantum dots synthesized by hot injection glow bright green and the emission range is between 500 and 550 nm (Figures S2 and S3, Supporting Information). However, the maximum absorption peak of the unmodified MAPbI₃ film is in the ultraviolet region and the

absorption capacity for green light is insufficient (Figure 2a). This mismatch between the emission of the scintillators and the absorption of the perovskite films results in low photocurrent and low sensitivity. Nevertheless, as a result of the high quality of the MAPbI₃ film and the high absorption coefficient of PDI-EAI, the emission range of CsPbBr₃ quantum dots was improved markedly after addition of PDI-EAI.

X-ray diffraction of MAPbI₃ films with and without PDI-EAI modification shows main peaks at 14.1°, 28.4°, and 31.9° assigned to the (110), (220), and (310) lattice planes of MAPbI₃ crystals, respectively (Figure 2b).^[8] The peak intensity increases rapidly after adding PDI-EAI molecules, and the full-width at half-maximum of the main peak decreases from 0.140° to 0.134° (Figure S4, Supporting Information). According to the Scherrer equation,^[9]

$$D = \frac{K\lambda}{B\cos\theta} \quad (2)$$

where D is the average size of the ordered crystalline domains, K is the dimensionless shape factor, λ is the X-ray wavelength, B is the full-width at half-maximum of the peak, and θ is the Bragg angle. The domain size of perovskite crystals increased from 57.8 to 62.3 nm. This improvement is due to the high crystallinity and high surface coverage of the PDI-EAI-modified film.

To validate whether PDI-EAI-modified perovskites are uniform and compact, the MAPbI₃ crystal film was analyzed by scanning electron microscopy (Figure 2c and Figure S5, Supporting Information). Some deep cracks and inhomogeneous grains were clearly observed in the pristine thin film, while the

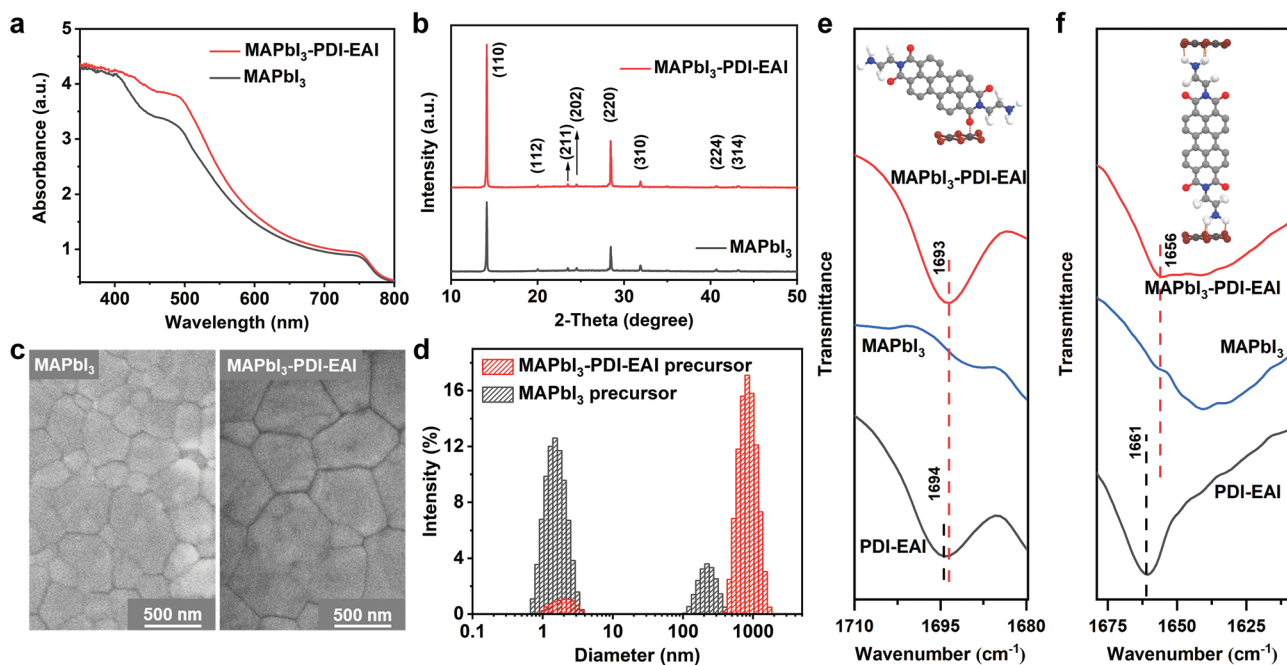


Figure 2. a) UV–vis absorption spectrum of non-PDI-EAI and PDI-EAI-modified MAPbI₃ films on the glass substrate. b) X-ray diffraction patterns the MAPbI₃ films on the glass substrate with and without PDI-EAI-modification. c) Top-view SEM images of MAPbI₃ films prepared on the Si substrate with and without PDI-EAI molecule. d) Dynamic light-scattering spectra of MAPbI₃ and MAPbI₃-PDI-EAI precursors. e,f) Fourier transform infrared spectra of PDI-EAI, MAPbI₃, and MAPbI₃-PDI-EAI precursors.

film prepared with PDI-EAI additive showed more compact arrangements and more uniform crystallites than the nonadditive film, which facilitated photon absorption as shown in the UV–vis absorption spectrum.

To study the reason for the increase in grain size in PDI-EAI-modified films, we measured the infrared spectroscopy spectrum of the perovskite precursor. The carbonyl vibration of the PDI-EAI solution is slightly redshifted after mixing with the perovskite (Figure 2e). This could be due to a coordination between the carbonyl group and Pb.^[10] In addition, the redshift of the peak of NH bond vibration demonstrates the interaction between PDI-EAI and the perovskite in dimethyl sulfoxide (Figure 2f). As a result, the iodoplumbate complexes (perovskite intermediates) are linked by PDI-EAI molecules and the cluster in PDI-EAI-doped precursor is larger than in the pure perovskite solution, as evidenced by dynamic light scattering measurements (Figure 2d). We found that the cluster size of PDI-EAI perovskite solution is ≈1000 times larger than that of the perovskite precursor, leading to high-quality MAPbI₃ thin films.^[11]

The carbonyl–Pb interaction can also be detected in the perovskite film by X-ray photoelectron spectroscopy (Figure S6, Supporting Information). Compared with the pristine film, the Pb4f_{7/2} peak of the PDI-EAI-modified sample shifted from 138.52 to 138.37 eV and the Pb4f_{5/2} peak shifted from 143.37 to 143.22 eV. This is because Pb atoms receive electrons from the carbonyl group. This interaction can passivate surface defects and reduce charge recombination in the perovskite film.^[12]

We next studied the photoluminescence spectra of MAPbI₃ films prepared on the glass substrate (Figure 3a). Owing to the charge transfer from perovskite to PDI-EAI, the photoluminescence intensity of the PDI-EAI-modified film is significantly

lower than that of the pure perovskite film. This increased photoluminescence-quenching yield of the PDI-EAI-containing sample provides a fast electron collection efficiency in the detector.^[13] Furthermore, a blue shift in fluorescence emission was observed after addition of PDI-EAI compared with the control film, implying that the PDI-EAI-modified perovskite film has fewer defects (Figure S7, Supporting Information).^[14] The low-defect density is beneficial for low dark current and low detection limit of the whole device.

The space charge-limited current under different bias voltages can be used to quantitatively evaluate the defect density and carrier mobility of MAPbI₃ films (Figure 3b and Figure S8, Supporting Information). Therefore, a device with the structure Ag/PCBM/MAPbI₃/SnO₂/ITO was fabricated to measure the current–voltage curve in the dark. The defect density can be calculated by the following equation:^[8]

$$N_{\text{defect}} = \frac{2\epsilon_0\epsilon V_{\text{TFL}}}{eL^2} \quad (3)$$

where ϵ_0 and ϵ are the vacuum permittivity and relative permittivity of MAPbI₃, respectively, V_{TFL} is the voltage of the dividing point between the ohmic contact and the trap-filled limit region, e is the elementary charge, and L is the thickness of the perovskite film. The defect density of the PDI-EAI-modified film is thereby $2.47 \times 10^{16} \text{ cm}^{-3}$, which is 15% lower than the value of the unmodified film. The electron mobility of the perovskite film can be determined using the Mott–Gurney equation:

$$\mu = \frac{8JL^3}{9\epsilon_0\epsilon V^2} \quad (4)$$

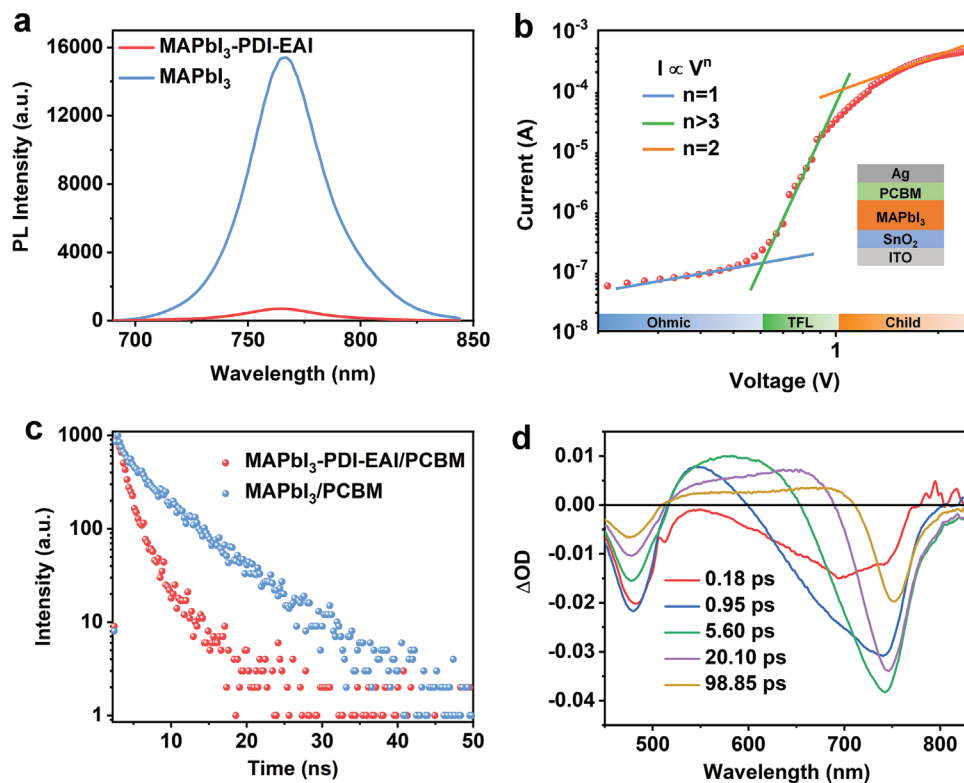


Figure 3. a) Steady-state photoluminescence spectra of the MAPbI₃ films with and without PDI-EAI additive. b) Space charge-limited current measurements of the electron-only devices. c) Time-resolution photoluminescence analysis of perovskite films with and without PDI-EAI-modification. d) 2D femtosecond transient absorption spectra of Δ OD versus wavelength at various time delay of PDI-EAI-modified sample.

where V is the bias voltage and J is the current density. Hence, the carrier mobility of MAPbI₃ films with PDI-EAI can reach $2.02 \times 10^{-5} \text{ cm}^2 \text{ V}^{-1} \text{ s}^{-1}$, which is nearly two times higher than the value of pristine films. This high electron mobility is due to the excellent electrical property of PDI-EAI and the high quality of MAPbI₃ films.

We further measured the time-resolved photoluminescence spectrum of MAPbI₃ films prepared on PCBM substrates (Figure 3c). The carrier lifetime can be obtained by fitting results with the biexponential decay function:^[15]

$$y = A_1 e^{-x/\tau_1} + A_2 e^{-x/\tau_2} + y_0 \quad (5)$$

$$\tau = \frac{A_1 \tau_1^2 + A_2 \tau_2^2}{A_1 \tau_1 + A_2 \tau_2} \quad (6)$$

where A_1 and A_2 are the relative amplitudes, and τ_1 and τ_2 are the lifetimes of fast and slow recombination, respectively. The unmodified film shows a lifetime of $\tau = 1.76 \text{ ns}$, whereas the PDI-EAI-modified film shows a shorter lifetime of $\tau = 1.09 \text{ ns}$, which can be ascribed to the better matching of energy levels among MAPbI₃, PDI-EAI, and PCBM as well as the high electron transfer efficiency from the perovskite to the additive then to the PCBM.^[15,16]

To further identify the carrier dynamics of perovskite films, we performed femtosecond transient absorption spectroscopy under 510 nm excitation (Figure 3d and Figure S9, Supporting Information). In a typical measurement, the

perovskite film was promoted to an electronically excited state by the pump beam, and the corresponding decay dynamics of the film's relative optical density (Δ OD) was then recorded as a function of wavelength and time delay. The positive Δ OD represents photo-induced absorption, and the negative Δ OD stands for ground-state bleaching.^[17] We found that the absolute intensity of the ground-state bleaching at $\approx 750 \text{ nm}$ is weaker for the PDI-EAI-modified film. This could be due to the charge transfer from MAPbI₃ to PDI-EAI molecules, resulting in fewer electrons occupying the conduction band minimum. The PDI-EAI-modified sample exhibited a new peak at 600–700 nm at the first 1 ps, which partially coincides with the ground-state bleaching of MAPbI₃. This peak may be caused by the ground-state bleaching of PDI-EAI molecules and PDI-EAI-coupled perovskites, which can lead to the larger width of negative peak of PDI-EAI-modified film than the pristine film.

A photodetector with the structure Ag/LiF/PCBM/MAPbI₃/PEDOT:PSS/ITO was fabricated to detect X-rays. The thickness of each layer is $\approx 80/\approx 1/\approx 50/\approx 400/\approx 50/\approx 150 \text{ nm}$. Then, $\approx 150 \mu\text{m}$ thick CsPbBr₃ quantum dots were coated on the ITO side to enhance the absorption and conversion of X-rays (Figure S10, Supporting Information). We next measured the current density versus time curve of the PDI-EAI-modified device with encapsulation under different dose rates of 20 keV X-rays (Figure 4a and Figure S11, Supporting Information). Both the photocurrent and dark current exhibited good stability and repeatability. The current response is highly linear with X-ray

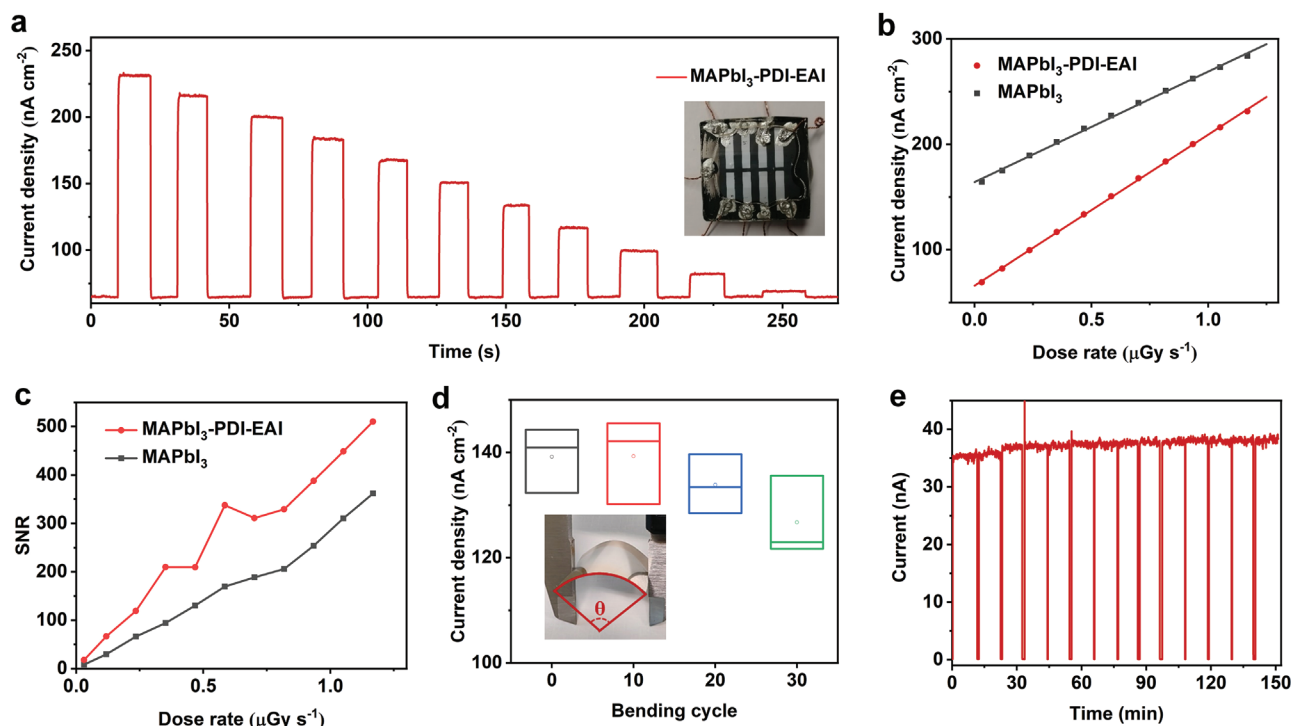


Figure 4. a) Photocurrent response of the PDI-EAI-modified device under zero bias voltage when exposed to 20 keV photon energy irradiation with different dose rates. b) X-ray photocurrent density as a function of dose rate. c) Signal-to-noise ratio of the unmodified device and the PDI-EAI-modified detector at different dose rates. d) Test of the flexible X-ray detector under repeated bending. e) Current response of the PDI-EAI-modified detector without encapsulation under 50 keV X-rays at 21°C and 72% relative humidity.

dose rate, which can facilitate system calibration and improve the accuracy of dose measurements (Figure 4b).^[18]

There are two key characteristics for high-performance X-ray detectors. One is high sensitivity (S), the other is low detection limit. Sensitivity directly reflects the ability of the detector to respond to radiation and electricity. It can be calculated as:

$$S = \frac{\Delta I}{D \cdot A} \quad (7)$$

where ΔI is the difference between photocurrent (I_{light}) and dark current (I_{dark}), D is the dose rate of incident radiation, and A is the effective irradiation area.^[19] Therefore, the slope of a linear fit of current density to dose rate is equal to the sensitivity of the detector. According to the photocurrent response curve, we can obtain an ultrahigh sensitivity of $143\,169 \pm 848 \mu\text{C Gy}_{\text{air}}^{-1} \text{cm}^{-2}$, which is over 7000 times higher than the value of commercial a-Se X-ray detectors ($20 \mu\text{C Gy}_{\text{air}}^{-1} \text{cm}^{-2}$, Figure 4b).

The detection limit is defined as the equivalent dose rate to generate a signal-to-noise ratio (SNR) that is at least 3. The SNR can be expressed by the following formula:

$$\text{SNR} = \frac{I_{\text{signal}}}{I_{\text{noise}}} = \frac{\bar{I}_{\text{light}} - \bar{I}_{\text{dark}}}{\sqrt{\frac{1}{N} \sum_i (I_i - \bar{I}_{\text{light}})^2}} \quad (8)$$

where \bar{I}_{light} and \bar{I}_{dark} are the average photocurrent and dark current, respectively.^[19,20] At a low dose rate of 30.77 nGy s^{-1} , the

PDI-EAI-modified detector still showed a high SNR of 1794 (Figure 4c). This low detection limit can be attributed to the low defect density and high responsivity of the PDI-EAI-modified device.

We next fabricated a flexible X-ray detector without encapsulation by replacing the glass substrate with the PET film (Figure S12, Supporting Information). The sensitivity of the PDI-EAI-modified device is $103\,097 \pm 2258 \mu\text{C Gy}_{\text{air}}^{-1} \text{cm}^{-2}$, while the value of the unmodified device is $90\,940 \pm 2473 \mu\text{C Gy}_{\text{air}}^{-1} \text{cm}^{-2}$ (Figure S13, Supporting Information). The PET film-based detector also showed a high SNR at a low-dose rate (Figure S14, Supporting Information). The output signal of the flexible device showed no significant attenuation at a bending angle of 120° , while at 180° the photocurrent decreased by $\approx 8\%$ and the dark current increased by over 160% (Figure S15, Supporting Information). This phenomenon is likely due to cracking in the film and a decrease in projected area decreases under extreme bending. We further measured the durability of the flexible device under bending (Figure 4d). The defect generated after 30 bending cycles decreased the photocurrent by $\approx 9\%$, which can be attributed to improved defect passivation and charge collection by PDI-EAI molecules at the grain boundary. The photocurrent of the PDI-EAI-modified flexible device without encapsulation was also measured under 50 keV X-rays at 21 °C and 72% relative humidity (Figure 4e). After a high dose of over 27 Gy irradiation, the output current of the flexible detector is still stable.

3. Conclusion

In summary, we have demonstrated that the addition of an electron acceptor molecule PDI-EAI to MAPbI₃ films can enhance light absorption and charge transfer in perovskite-based detectors. By integrating PDI-EAI with perovskites, MAPbI₃ thin films can be improved in both surface morphology and green light absorption, resulting in an X-ray sensitivity of $143\,169 \pm 848\ \mu\text{C Gy}_{\text{air}}^{-1}\text{ cm}^{-2}$ and a detection limit of $30.77\ \text{nGy s}^{-1}$. Owing to the defect passivation and charge collection of PDI-EAI molecules, the device exhibits good durability against bending. Unlike most X-ray detectors, this device does not require any external power to operate, making it ideal for long-term environmental monitoring.

4. Experimental Section

The experimental details are provided in the Supporting Information.

Supporting Information

Supporting Information is available from the Wiley Online Library or from the author.

Acknowledgements

This research was primarily funded through the Agency for Science, Technology and Research (A*STAR) under its AME program (grant No. A1983c0038), National Research Foundation, and the Prime Minister's Office of Singapore under its Competitive Research Program (CRP Award No. NRF-CRP23-2019-0002), and NRF Investigatorship Programme (Award No. NRF-NRFI05-2019-0003).

Conflict of Interest

The authors declare no conflict of interest.

Data Availability Statement

The data that support the findings of this study are available in the Supporting Information of this article.

Keywords

defect passivation, flexible devices, high sensitivity, perylene diimide derivatives, X-ray detectors

Received: November 10, 2022

Revised: December 28, 2022

Published online:

- [1] a) Y. R. Su, W. B. Ma, Y. Yang, *J. Semicond.* **2020**, *41*, 051204; b) Y. Zhang, R. Sun, X. Ou, K. Fu, Q. Chen, Y. Ding, L. Xu, L. Liu, Y. Han, A. V. Malko, X. Liu, H. Yang, O. M. Bakr, H. Liu, O. F. Mohammed, *ACS Nano* **2019**, *13*, 2520.

- [2] a) Q. S. Chen, J. Wu, X. Y. Ou, B. L. Huang, J. Almutlaq, A. A. Zhumekenov, X. W. Guan, S. Y. Han, L. L. Liang, Z. G. Yi, J. Li, X. J. Xie, Y. Wang, Y. Li, D. Y. Fan, D. B. L. Teh, A. H. All, O. F. Mohammed, M. Bakr, O. T. Wu, M. Bettinelli, H. H. Yang, W. Huang, X. G. Liu, *Nature* **2018**, *561*, 88; b) F. G. Zhou, Z. Z. Li, W. Lan, Q. Wang, L. M. Ding, Z. W. Jin, *Small Methods* **2020**, *4*, 2000506; c) F. Maddalena, L. Tjahjana, A. Z. Xie, Arramel, S. W. Zeng, H. Wang, P. Coquet, W. Drozdowski, C. Dujardin, C. Dang, M. D. Birowosuto, *Crystals* **2019**, *9*, 88; d) B. Yang, L. Yin, G. Niu, J.-H. Yuan, K.-H. Xue, Z. Tan, X.-S. Miao, M. Niu, X. Du, H. Song, E. Lifshitz, J. Tang, *Adv. Mater.* **2019**, *31*, 1904711.
- [3] a) J. Y. Liu, B. Shabbir, C. J. Wang, T. Wan, Q. D. Ou, P. Yu, A. Tadich, X. C. Jiao, D. W. Chu, D. C. Qi, D. B. Li, R. F. Kan, Y. M. Huang, Y. M. Dong, J. Jasieniak, Y. P. Zhang, Q. L. Bao, *Adv. Mater.* **2019**, *31*, 1901644; b) X. Ou, X. Qin, B. Huang, J. Zan, Q. Wu, Z. Hong, L. Xie, H. Bian, Z. Yi, X. Chen, Y. Wu, X. Song, J. L. Li, Q. Chen, H. Yang, X. Liu, *Nature* **2021**, *590*, 410; c) M. Dustler, D. Föhrnvik, P. Timberg, S. Zackrisson, S. Muller, *Acta Radiol.* **2021**, *62*, 1583.
- [4] a) S. Yakunin, M. Sytnyk, D. Kriegner, S. Shrestha, M. Richter, G. J. Matt, H. Azimi, C. J. Brabec, J. Stangl, M. V. Kovalenko, W. Heiss, *Nat. Photonics* **2015**, *9*, 444; b) A. Popoola, M. A. I. K. Gondal, Popoola, L. E. O. , O. M. Bakr, *Org. Electron.* **2020**, *84*, 105730; c) W. Yang, W. Qiu, E. Georgitzikis, E. Simoen, J. Serron, J. Lee, I. Lieberman, D. Cheyins, P. Malinowski, J. Genoe, *ACS Appl. Mater. Interfaces* **2021**, *13*, 16766; d) J. Chen, N. Shirahata, H. Sun, *Nat. Photonics* **2021**, *15*, 171.
- [5] Y. C. Chiang, C. C. Hung, Y. C. Lin, Y. C. Chiu, T. Isono, T. Satoh, W. C. Chen, *Adv. Mater.* **2020**, *32*, 2002638.
- [6] a) S. Koyuncu, H.-W. Wang, F. Liu, K. B. Toga, W. Gu, T. P. Russell, *J. Mater. Chem. A* **2014**, *2*, 2993; b) C. Garcias-Morales, D. Romero-Borja, J.-L. Maldonado, A. E. Roa, M. Rodríguez, J. P. García-Merinos, A. Ariza-Castolo, *Molecules* **2017**, *22*, 1607.
- [7] a) Z. Zhu, Q. Xue, H. He, K. Jiang, Z. Hu, Y. Bai, T. Zhang, S. Xiao, K. Gundogdu, B. R. Gautam, H. Ade, F. Huang, K. S. Wong, H.-L. Yip, S. Yang, H. Yan, *Adv. Sci.* **2016**, *3*, 1500; b) J. Y. Huang, E.-W. Chang, Y. R. Wu, *IEEE J. Photovolt.* **2019**, *9*, 1686; c) Y. C. Wang, Y. M. Zhang, Y. T. Liu, T. Q. Pang, Z. Y. Hu, Y. J. Zhu, S. Z. Luan, R. X. Jia, *J. Phys. D* **2017**, *50*, 475101.
- [8] a) H. Zhao, S. R. Wang, M. N. Sun, F. Zhang, X. G. Li, Y. Xiao, *J. Mater. Chem. A* **2018**, *6*, 10825; b) W. Yu, F. Li, L. Yu, M. R. Niazi, Y. Zou, D. Corzo, A. Basu, C. Ma, S. Dey, M. L. Tietze, U. Buttner, X. Wang, Z. Wang, M. N. Hedhili, C. Guo, T. Wu, A. Amassian, *Nat. Commun.* **2018**, *9*, 5354.
- [9] a) H. Peng, Z. Su, Z. Zheng, H. Lan, J. Luo, P. Fan, G. Liang, *Materials* **2019**, *12*, 1237; b) W. Peng, L. Wang, B. Murali, K. Ho, A. Bera, N. Cho, C. Kang, V. M. Burlakov, J. Pan, L. Sinatra, C. Ma, W. Xu, D. Shi, E. Alarousu, A. Goriely, J. He, O. F. Mohammed, T. Wu, O. M. Bakr, *Adv. Mater.* **2016**, *28*, 3383.
- [10] T. Wu, Y. Wang, X. Li, Y. Wu, X. Meng, D. Cui, X. Yang, L. Han, *Adv. Energy Mater.* **2019**, *9*, 1803766.
- [11] a) Y. Zhang, Y. Wang, X. Yang, L. Zhao, R. Su, J. Wu, D. Luo, S. Li, P. Chen, M. Yu, Q. Gong, R. Zhu, *Adv. Mater.* **2022**, *34*, 2107420; b) X. Hou, S. M. Huang, O. Y. Wei, L. K. Pan, Z. Sun, X. H. Chen, *ACS Appl. Mater. Interfaces* **2017**, *9*, 35200; c) L. Liu, K. Pan, K. Xu, J. Z. Zhang, *ACS Phys. Chem. Au.* **2022**, *2*, 156.
- [12] Z. Wu, M. Jiang, Z. Liu, A. Jamshaid, L. K. Ono, Y. Qi, *Adv. Energy Mater.* **2020**, *10*, 1903696.
- [13] F. Zhang, W. Shi, J. Luo, N. Pellet, C. Yi, X. Li, X. Zhao, T. J. S. Dennis, X. Li, S. Wang, *Adv. Mater.* **2017**, *29*, 1606806.
- [14] a) M. Sun, F. Zhang, H. Liu, X. Li, Y. Xiao, S. Wang, *J. Mater. Chem. A* **2017**, *5*, 13448; b) Z. Tan, J. Li, C. Zhang, Z. Li, Q. Hu, Z. Xiao, T. Kamiya, H. Hosono, G. Niu, E. Lifshitz, Y. Cheng, J. Tang, *Adv. Funct. Mater.* **2018**, *28*, 1801131; c) M.-F. Yang, J.-P. Yang, *Appl. Phys. Lett.* **2020**, *117*, 071602; d) Z. Tan, Y. Chu, J. Chen, J. Li, G. Ji, G. Niu, L. Gao, Z. Xiao, J. Tang, *Adv. Mater.* **2020**, *32*, 2002443.

- [15] J. You, L. Meng, T.-B. Song, T.-F. Guo, Y. M. Yang, W.-H. Chang, Z. Hong, H. Chen, H. Zhou, Q. Chen, *Nat. Nanotechnol.* **2016**, *11*, 75.
- [16] K. Jiang, F. Wu, H. Yu, Y. Yao, G. Zhang, L. Zhu, H. Yan, J. *Mater. Chem. A* **2018**, *6*, 16868.
- [17] a) E. Serpetzoglou, I. Konidakis, G. Kakavelakis, T. Maksudov, E. Kymakis, E. Stratakis, *ACS Appl. Mater. Interfaces* **2017**, *9*, 43910; b) M. Zhou, J. S. Sarmiento, C. Fei, H. Wang, *J. Phys. Chem. C* **2019**, *123*, 22095.
- [18] a) A. J. Fleming, *Sens. Actuator A Phys.* **2013**, *190*, 106; b) R. A. Lewis, *Phys. Med. Biol.* **2004**, *49*, 3573; c) J. Pang, S. Zhao, X. Du, H. Wu, G. Niu, J. Tang, *Light Sci. Appl.* **2022**, *11*, 105; d) J. Wang, X. Wang, J. Yin, L. Gutiérrez-Arzaluz, T. He, C. Chen, Y. Han, Y. Zhang, O. M. Bakr, M. Eddaoudi, O. F. Mohammed, *ACS Energy Lett.* **2022**, *7*, 10.
- [19] a) Y. X. Zhang, Y. C. Liu, Z. Xu, H. C. Ye, Z. Yang, J. X. You, M. Liu, Y. H. He, M. G. Kanatzidis, S. Z. Liu, *Nat. Commun.* **2020**, *11*, 2304; b) L. Yao, G. Niu, L. Yin, X. Du, Y. Lin, X. Den, J. Zhang, J. Tang, *J. Mater. Chem. C* **2020**, *8*, 1239.
- [20] L. Basirico, A. Ciavatti, B. Fraboni, *Adv. Mater. Technol.* **2021**, *6*, 2000475.